Impact of density gradients on secondary flow structure at a river confluence

J. Duguay[1], P. M. Biron[1], J. Lacey[2]

[1]Department of Geography, Planning and Environment, 1455 De Maisonneuve Blvd. W., Montreal, QC, Canada

[2]Department of Civil Engineering, Université de Sherbrooke, 2500 boul. de l'Université, Sherbrooke, QC, Canada

Key Points:

- The direction of the density difference dictates the sense of rotation of the streamwise orientated vorticity in the mixing interface.
- For a given magnitude of $\Delta\rho$, the inertia of the light channel dictates whether coherent density SOVs or interfacial instabilities form.
- A densimetric Froude convention considering the direction of $\Delta\rho$ is proposed to convey the interaction of density and inertial effects.

Corresponding author: J. Duguay, j_dug@live.concordia.ca

Abstract

A small gradient in the densities ($\Delta\rho$) of two rivers was recently shown to develop coherent streamwise orientated vortices (SOVs) in the mixing interface of their confluence. We further investigate this phenomenon at the Coaticook and Massawippi confluence (Quebec, Canada) using eddy-resolved numerical modelling to examine how the magnitude and direction of $\Delta\rho$ affect this secondary flow feature. Results show that a front from the denser channel always slides underneath the lighter channel independent of the direction of $\Delta\rho$. When the fast tributary (Coaticook) is denser, coherent clockwise rotating density SOVs tend to form on the slow (Massawippi) side. However, when the slow Massawippi is denser by the same magnitude, anticlockwise secondary flow caused principally by shear induced interfacial instabilities develop on the fast Coaticook side. This shows the inertia of the tributary opposing the lateral propagation of the dense front shapes the secondary flow characteristics of the mixing interface. Moreover, in the absence of a density difference, anticlockwise SOVs are predicted by the model which correspond well to new aerial observations of anticlockwise SOVs at the site. A densimetric Froude number ($\mathbf{F}_D$) convention accounting for the direction of $\Delta\rho$ is proposed to accurately convey the local inertial forces that oppose the lateral propagation of the dense front. Finally, a conceptual model of the mixing interface's secondary flow structure over a spectrum of plausible $\mathbf{F}_D$ values is proposed. The $\mathbf{F}_D$ convention provides a flexible and consistent metric for use in future studies examining the effects of $\Delta\rho$ on river confluence hydrodynamics.

1 Introduction

Coherent flow structures affect mixing processes at river confluences and therefore influence water and habitat quality downstream (Best, 1987; P. Biron et al., 1996; Rhoads & Sukhodolov, 2001; Sukhodolov & Rhoads, 2001; Lyubimova et al., 2014; Constantinescu et al., 2016; Rhoads, 2020; van Rooijen et al., 2020). A greater understanding of these structures is of interest to better predict the impact of tributaries on downstream reaches. Four forms of coherent flow structures are often discussed: helical cells (secondary flow at the scale of the tributaries' widths), vertically orientated Kelvin-Helmholtz (KH) vortices (shear-induced instabilities along the mixing interface), episodic pulses (origins still not fully understood, see Sabrina et al. (2021)) and streamwise orientated vortices (SOVs). SOVs were first discovered in numerical models as a pair of back-to-back, counter-rotating SOVs, each revolving around the streamwise axis on both sides of the mixing interface of a river

confluence (Constantinescu et al., 2011). Their development is generally attributed to the downwelling of superelevated flow in the collision zone caused by the converging rivers, in a process strengthened by superelevation caused by planform curvature (Sukhodolov & Sukhodolova, 2019). Recently, however, strongly coherent SOVs were directly observed in the movements of turbidity gradients at the Coaticook-Massawippi confluence in aerial drone video (Quebec, Canada, Duguay et al. (2022) and numerical modelling has suggested these SOVs were actually a gravity current caused by a small density gradient $\Delta\rho$ of ≈ 0.5 kg/m^3 (Coaticook was denser) confined between the converging rivers (Duguay et al., 2022). The sensitivity of these secondary flow structures to larger magnitudes of $\Delta\rho$ and/or a reversal in the direction of $\Delta\rho$ has yet to be examined.

Density gradients occur when differences in temperature, dissolved minerals or suspended sediment concentrations are present across the mixing interface. Such gradients are common at river confluences (P. M. Biron & Lane, 2008; Lane et al., 2008; Lyubimova et al., 2014; van Rooijen et al., 2020) and cause the converging flows to stratify; where increasing $\Delta\rho$ induces greater stratification and surface area for turbulent mixing exchanges (P. M. Biron & Lane, 2008; Ramón et al., 2014; Cheng & Constantinescu, 2018; van Rooijen et al., 2020). The analogy of a spatially developing lock-exchange is often used to convey how $\Delta\rho$ affects the bulk properties of a confluence's mixing interface (Cheng & Constantinescu, 2018; Horna-Munoz et al., 2020; Jiang et al., 2022), however, the suitability of this analogy is questionable.

The dynamics of turbid SOVs observed in a drone video of the Coaticook-Massawippi confluence presented by Duguay et al. (2022) could only be reproduced with an eddy-resolved model when the Coaticook was 0.5 kg/m^3 denser than the Massawippi. This small magnitude of $\Delta\rho$, though adequate to affect secondary flow structure, did not develop the typical vertical stratification of a lock-exchange flow, but instead produced a strongly coherent streamwise oriented vortex. This departure from expectations led to the realisation that the observed SOVs were instead a *confined* gravity current - a continuous 3D process initiated by the $\Delta\rho$ induced hydrostatic pressure gradient at the confluence's apex. The pressure gradient forces a front of denser water to extend laterally along the bed which causes a front of the lighter fluid to flow in the opposite direction near the surface to replace the 'falling' dense tributary. This cross-flow is similar to the dense and light fronts of a lock-exchange in the initial moments after its release (Rottman & Simpson, 1983; Cantero et al., 2007). However, where the fronts encounter sufficient opposing momentum from the

adjacent tributary, the dense front is deflected back above itself and the light front deflects downwards as it collides with the denser tributary. The resulting confined cross-flow (i.e. gravity current) produces a coherent density SOV which advects and accelerates down the mixing interface with the streamwise flow component (see Video 1 and Duguay et al. (2022)).

The interaction of density induced secondary flow features with the inertial forces present at a confluence are little understood. Nevertheless, results from previous studies suggests that these interactions should vary along a spectrum depending on the relative strength of inertial to density induced buoyant forces (P. M. Biron & Lane, 2008; Ramón et al., 2014; Cheng & Constantinescu, 2018; Gualtieri et al., 2019; van Rooijen et al., 2020; Horna-Munoz et al., 2020). At the weak end, nearly complete stratification should develop when buoyant forces dominant, for example when little lateral momentum opposes the spread of the dense front. Farther along the spectrum, density SOVs result as buoyant forces are still sufficient for the dense front to extend, yet are too weak to extend the front farther than a few depths into the opposing flow (Duguay et al., 2022). Even farther along the spectrum, the increasing inertia of the opposing tributary should shear the dense front, developing interfacial instabilities similar to those mentioned by Horna-Munoz et al. (2020). Finally, a near vertical mixing interface will develop when the inertial forces of a very fast opposing tributary dominate buoyant forces. However, where on the spectrum these transitions occur and the intermediary states of the mixing interface between them have not been explored.

The metric used to assess the relation between density and inertial effects on confluence hydrodynamics is the densimetric Froude number $\mathbf{F}_D$:

$$\mathbf{F}_D = \frac{U_0}{\sqrt{g' D}} \tag{1}$$

$$g' = \frac{(\rho_1 - \rho_2)}{\rho_1} g \tag{2}$$

where g' is reduced gravity (Eq. 2, g is the constant of gravitational acceleration, ρ_1 and ρ_2 are respectively the densities of the denser and lighter tributaries), D is a characteristic depth and U_0 is a characteristic velocity (Rhoads, 2020).

As discussed by Rhoads (2020) and, emphasised with respect to the Coaticook-Massawippi confluence in Duguay et al. (2022), consensus on a convention for U_0 and depth D in Eq. 1 has not been achieved - leading to ambiguous interpretations of $\mathbf{F}_D$ and consequently difficulties applying it as a consistent metric to predict density/inertial effect interactions. The ensuing confusion is best illustrated with a recent excerpt from the literature. For instance, Jiang et al. (2022) state: "Given that the corresponding densimetric Froude number ($\mathbf{F}_D = 1/Ri^{0.5} = 5.2$) is less than 10, one expects density contrast effects to be fairly significant (Horna-Munoz et al., 2020) (p. 7)". However, in the cited article (i.e. Horna-Munoz et al. (2020)) those authors describe a case with a $\mathbf{F}_D = 4.9$ as having "weak-density-effects" and one with $\mathbf{F}_D = 1.6$ as "strong-density-effects". Thus, a value of $\mathbf{F}_D$ of 5.2 is considered significant by Jiang et al. (2022), whereas a similar value of 4.9 is considered weak by Horna-Munoz et al. (2020). A researcher interpreting such contrasting statements in the context of a new confluence will be left confused and possibly questioning whether $\mathbf{F}_D$ is a meaningful metric at all.

Outside its application to confluences, $\mathbf{F}_D$ is generally used to relate the proportion of buoyant to inertial forces acting on submerged bodies in a rectilinear velocity field. For example, ocean currents opposing heavy saline gravity currents in marine environments (Dorrell et al., 2016), rivers carrying sediment particles longitudinally as they fall to the bed (Aguirre-Pe et al., 2003) or frazil ice flocks rising to the surface of rivers in cold climates (Lindenschmidt, 2017). In such scenarios U_0 is taken as the depth averaged velocity and, D either the body's diameter or the flow depth. However, at a confluence the presence of two rivers with different velocities and depths complicates the choice of U_0 and D. Historically this difficulty has generally been overlooked as $\mathbf{F}_D$ is usually calculated using bulk values of U_0 and D taken at a cross-section through the mixing interface or in the main channel (Table 1) with no physically derived rational to support the choice. Importantly, as discussed by Duguay et al. (2022) definitions of $\mathbf{F}_D$ based on such bulk flow properties lack the subtlety necessary to account for the direction of $\Delta\rho$, or more explicitly - the inertial effects with which the light channel opposes the lateral propagation of the dense front.

Considering the impact of $\Delta\rho$ on the secondary flow field noted by Duguay et al. (2022) and the fact that such small values of $\Delta\rho$ (e.g. < 2 kg/m^3) commonly occur at confluences (Rhoads & Sukhodolov, 2001; Cook & Richmond, 2004; P. M. Biron & Lane, 2008; Lane et al., 2008; van Rooijen et al., 2020), a greater understanding of how density induced secondary flow structures react to the direction and magnitude of $\Delta\rho$ and an improved

Table 1. Velocity and length scales used to calculate $\mathbf{F}_D$ in previous studies

Reference	U_0	D
Ramón et al. (2016)	inflow velocity of main channel	simply "depth"
Cheng and Constantinescu (2018)*	either "average velocity of both tributaries close to the confluence" (p. 4543) or "mean velocity of main channel" (p. 4540). Not clear.	average depth of main channel
Gualtieri et al. (2019)	"average velocity at the beginning of the confluence"	"median cross sectional depth" at the beginning of the confluence
Cheng and Constantinescu (2019)*	mean velocity of main channel	mean depth in main channel
Horna-Munoz et al. (2020)	discharge-weighted average of the bulk velocities of the tributaries	mean depth in the center of the confluence
van Rooijen et al. (2020)	simply "mean velocity"	height of the density current
Cheng and Constantinescu (2021)	mean velocity of downstream channel	mean flow depth downstream channel
Jiang et al. (2022)	simply "area averaged streamwise velocity"	mean flow depth in the main channel downstream of the apex

Notes: * indicates Richardson number $R_i{=}g'D/U_0^2$ was calculated instead which is equivalent to $\mathbf{F}_D^{-2}$.

definition of $\mathbf{F}_D$ are required if an accurate conceptual model of confluence hydrodynamics is to be achieved. Towards this end, we analyse a set of eddy-resolved numerical simulations of the Coaticook-Massawippi confluence. The simulations use constant hydraulic conditions, yet consider various combinations of the magnitude and direction of $\Delta\rho$. A conceptual model summarising density and inertial effects on the secondary flow field of the mixing interface is discussed and a modified definition of $\mathbf{F}_D$ is proposed which accurately conveys these effects.

2 Methods

2.1 Field site

The Coaticook-Massawippi confluence and hydraulic conditions studied herein are the same as those studied and described in Duguay et al. (2022). Details of the confluence and the methods used to evaluate its planform geometry, bathymetry, sediment grain sizes, discharges and depths are also described in Duguay et al. (2022) so only the key features are repeated here. At discharges of $Q > 15$ m^3/s, the Coaticook (tributary), located in an agricultural watershed (514 km^2), carries a high concentration of suspended sediment (e.g. > 200 mg/l). In contrast, the Massawippi (main channel, watershed area of 610 km^2), which flows from Lake Massawippi through a mostly wooded portion of its watershed for 9.6 km, is generally clear (< 30 mg/l). The resulting turbidity contrast provides excellent aerial views of coherent flow structures in the mixing interface. Clear examples of strongly coherent density SOVs were observed in aerial drone video at the meander-bend confluence on July 9^{th}, 2020 and are described in detail in Duguay et al. (2022). Details of the confluence on this day are depicted in Fig. 1 and flow conditions in Table 1.

2.2 Simulated density variations

A set of 7 eddy-resolved simulations (cases) were performed to investigate the effects of the magnitude and direction of $\Delta\rho$ on the coherent flow structure of the confluence's mixing interface. The same numerical model detailed in Duguay et al. (2022) was used in each case with the hydraulic conditions of July 9^{th} 2020. The discharge and water surface level in each case were constant (Table 2), however, the direction and magnitude of $\Delta\rho$ were varied. A notation is adopted conveying both the magnitude and direction of $\Delta\rho$. On July 9^{th}, 2020 the Coaticook was estimated to be 0.5 kg/m^3 denser than the Massawippi (see

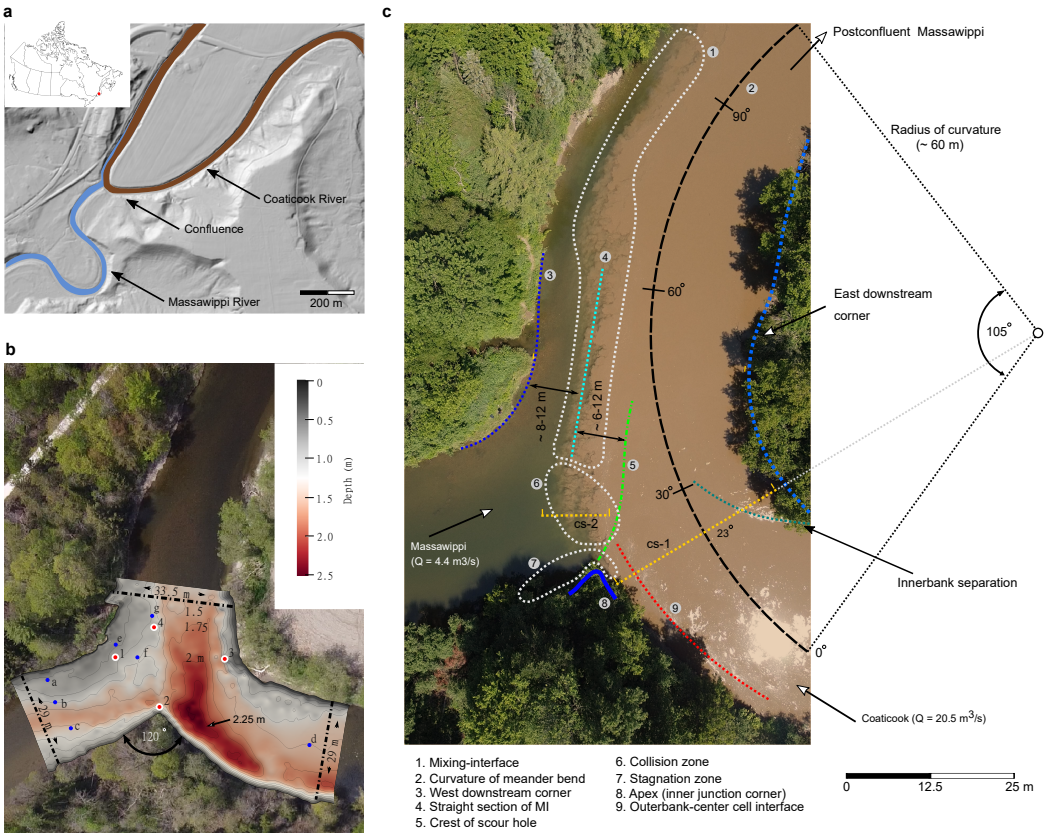

Figure 1. Massawippi-Coaticook meander-bend confluence. **a**, High-elevation planform geometry of the confluence located in the province of Quebec, Canada (45°18'50"N 71°53'55"W). At high discharge, the Coaticook, which flows through an agricultural watershed is generally turbid. The Massawippi, flowing through a forested watershed is often clear. **b**, Planform characteristics and hydrodynamic zones on an aerial view of the confluence taken on July 9^{th}, 2020. **c**, Bathymetry of the confluence coloured by depth below the free surface (146.07 m above sea level) during the numerical model validation field campaign of October 22^{nd}. 2020 (see Duguay et al. (2022)). Water surface elevation was 0.07 m higher on July 9^{th} than on October 22^{nd}, 2020. Contoured region delimits extents of the numerical modelling domain. Figure reproduced with permission from Fig. 1 of Duguay et al. (2022).

Table 2. Hydraulic conditions during SOV observations on July 9^{th}2020

Date	boundary	Q	B	A	h_{max}	ρ^*	H	U_{av}	**Fr**	**Re**
July 9^{th}, 2020 - $M_r = 16.9$										
	Massawippi	4.4	29.1	34.4	1.6	996.92	1.19	0.13	0.04	153400
	Coaticook	20.5	29.2	44	1.91	997.42	1.50	0.47	0.12	700300
	outlet	24.9	33.8	39.3	1.42		1.02	0.63	0.19	730800

Notes: Values derived from discharges measured at gauging stations upstream, water surface levels measured during the observations and bathymetric data gathered in the summer of 2020 (see Duguay et al. (2022) for details). Values pertain to the inlet and outlet cross-sections of the numerical model's domain. Q discharge (m^3/s), B width (m), A wetted area (m^2), h_{max} maximum depth (m), ρ^* estimated density (see subsection River densities and simulated cases in Duguay et al. (2022)), H average cross-sectional depth (m), U_{av} average cross-sectional velocity (m/s), **Fr** is the Froude number ($\mathbf{Fr} = U_{av}/\sqrt{gH}$), **Re** is the Reynolds number ($\mathbf{Re} = HU_{av}/\nu$). Momentum ratio, $M_r = \rho_C Q_C U_{av}^C / \rho_M Q_M U_{av}^M$ (subscript $_C$ for Coaticook, $_M$ for Massawippi).

Duguay et al. (2022)) and because the dense Coaticook is the right-hand tributary, density decreased across the mixing interface from right to left. We denote this as $\overleftarrow{\Delta\rho}$, where the arrow points in the lateral direction of decreasing density. Therefore, a left arrow indicates a denser Coaticook and a right arrow a denser Massawippi. A subscript is added to represent the magnitude of $\Delta\rho$, for example $\overleftarrow{\Delta\rho}_{0.5}$ shows the Coaticook is 0.5 kg/m^3 denser than the Massawippi. Table 3 presents the density conditions of the 7 cases. We have deliberately not referred to our cases in terms of the common definitions of the densimetric Froude number ($\mathbf{F}_D$) due to the difficulties that arise during their interpretation as discussed by (Duguay et al., 2022). However, we revisit $\mathbf{F}_D$ values based on a newly proposed definition in section 4.5.

2.3 Numerical model

The numerical model is identical to that of Duguay et al. (2022) and we refer the reader to that work for complete details including the equations solved, the construction of the mesh

Table 3. Density conditions of the numerical cases

case	ρ_M (kg/m^3)	ρ_C (kg/m^3)	$\Delta\rho$ (kg/m^3)
$\overleftarrow{\Delta\rho}_{2.0}$	996.92	998.92	2.00
$\overleftarrow{\Delta\rho}_{1.0}$	996.92	997.92	1.00
$\overleftarrow{\Delta\rho}_{0.5}$	996.92	997.42	0.50
$\Delta\rho_{0.0}$	996.92	996.92	0.00
$\overrightarrow{\Delta\rho}_{0.5}$	997.42	996.92	0.50
$\overrightarrow{\Delta\rho}_{1.0}$	997.92	996.92	1.00
$\overrightarrow{\Delta\rho}_{2.0}$	998.92	996.92	2.00

and the validation of the model with field data taken on October 22^{nd} 2020. A basic description of the model follows. The confluence's hydrodynamics were simulated by solving the incompressible continuity and Navier-Stokes equations using a wall-modelled large-eddy simulation (WMLES) with OpenFOAM's (v2012) *twoLiquidMixingFoam* solver. OpenFOAM is an open-sourced computational fluid dynamics code based on the finite volume method (Weller et al., 1998; Moukalled et al., 2016). OpenFOAM's *twoLiquidMixingFoam* solver and has been extensively validated for simulating buoyancy driven mixing of two fluids of different density (Gruber et al., 2011; Lai et al., 2015; Zhang et al., 2016; Grbčič et al., 2019) and uses a fluid fraction method (α) to determine ρ resulting from the mixing of two miscible fluids of different density. Flow of the Coaticook (subscript 1) is considered $\alpha = 1$ and that of the Massawippi $\alpha = 0$ (subscript 2). Practically, fractional values of α indicate the proportional volume of each cell originating from the Coaticook. The distribution of α is calculated using an advection-diffusion equation (Eq. 3, $\boldsymbol{u}$ velocity field, t time, D_{ab} molecular diffusivity between miscible fluids a and b, S_c is the turbulent Schmidt number). The dynamic viscosity (μ) and density at each computational cell are determined as fluid fraction weighted averages using Eqs. 3, 4 and 5.

$$\frac{\partial \alpha}{\partial t} + \nabla \cdot (\mathbf{u}\alpha) = \nabla \cdot \left(\left(D_{ab} + \frac{\nu_t}{S_c} \right) \nabla \alpha \right) \tag{3}$$

$$\rho = \rho_1 \alpha + \rho_2 (1 - \alpha) \tag{4}$$

$$\mu = \mu_1 \alpha + \mu_2 (1 - \alpha) \tag{5}$$

2.4 Simulations, initial conditions and stationarity

The flow field from the final time-step of a long duration (2000 s) coarse grid simulation of the $\Delta\rho_{0.0}$ case was mapped to a fine 36 million cell mesh as its initial conditions. The fine mesh was run for 1000 s before recording data for analysis. This 1000 s spin-up period ensured flow field artefacts from the initial conditions had sufficient time to exit the domain (only requiring $\approx$ 200 s) and for the flow field to attain a stationary regime. Considering the average cross-sectional velocity of 0.63 m/s at the outlet and a domain length of $\approx$ 65 m, the spin-up period equates to $\approx$ 10 flow-through periods. Statistical stationarity was assessed by performing an Augmented Dickey-Fuller (ADF) unit test on velocity time-series at various locations throughout the domain for the final 800 s of the spin-up period. ADF statistics indicated no long-duration trends (ADF statistics $p < 0.001$). Furthermore, first and second order turbulent statistics of 10 randomly selected 300 s segments extracted from the retained 800 s period also closely approximated the global values acquired over the 800 s period. After the 1000 s spin-up period, the $\Delta\rho_{0.0}$ was run for an additional 600 s, over which temporally averaged quantities were measured for analysis.

Cases considering $\Delta\rho$ used the final time-step of the 1000 s spin-up period of the $\Delta\rho_{0.0}$ case as initial conditions. However, for each value of $\Delta\rho$ tested, a second spin-up period was necessary to permit the flow field to adjust to the newly imposed $\Delta\rho$. This period was assessed by examining velocity time-series sampled in the mixing interface of the $\overleftarrow{\Delta\rho}_{2.0}$ case (i.e., the greatest magnitude of $\Delta\rho$ studied). Qualitatively, the adjustment of the mixing interface required $\approx$ 100 s to complete, after which the flow entered a stationary state. Quantitatively, velocity time series were monitored at points in the mixing interface. Figure 2 presents time series of the velocity components taken at mid-distance along the mixing interface. The first 100 s consist of the principal adjustment period and the next 200 s correspond to the residual adjustment period. The turbulent character of the principal adjustment period differs significantly from the remainder of the time series. Based on this analysis, a 300 s spin-up period was run in each simulation prior to flow field sampling. Each simulation was then run for an additional 600 s for data collection purposes. Instantaneous results were recorded every 2 s during the final 300 s for the production of figures and animations.

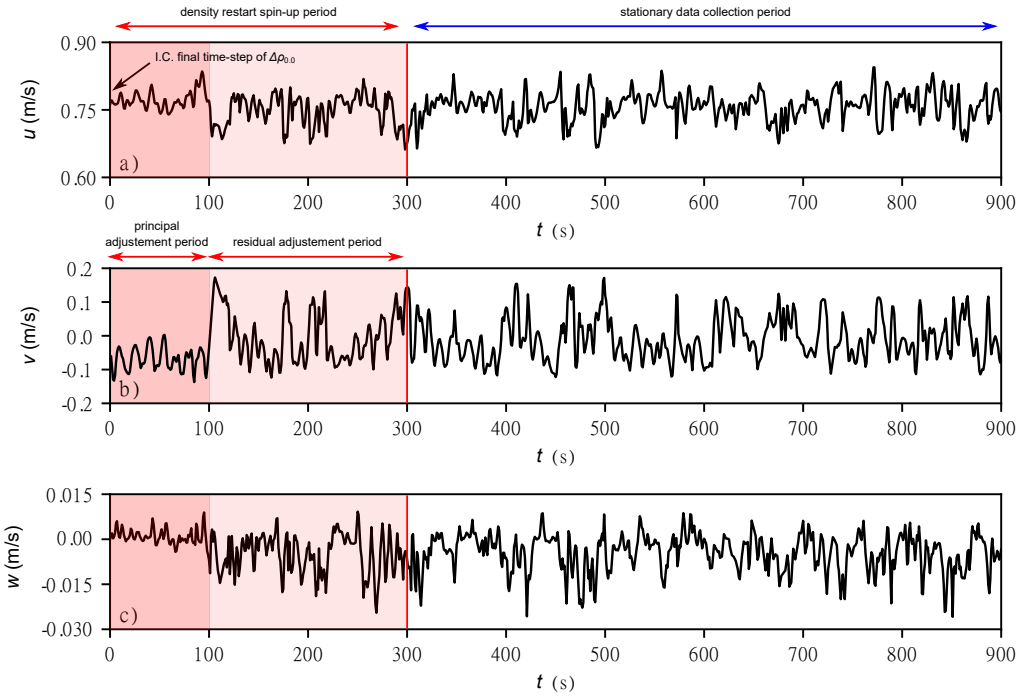

Figure 2. Time series of u, v and w sampled from numerical data at a point near the surface at mid-length along the mixing interface of the $\overleftarrow{\Delta\rho}_{2.0}$ case. The first 100 s correspond to the primary adjustment period necessary for the mixing interface to adjust from that of the $\Delta\rho_{0.0}$ to that of $\overleftarrow{\Delta\rho}_{2.0}$. The preceding 200 s corresponds to the residual adjustment period and the white zone indicates the portion of the simulation retained for analysis.

2.5 Model validation

The model was validated against field measurements obtained on October 22^{nd}, 2020. The validation, detailed in Duguay et al. (2022), supports that the numerical approach could accurately reproduce the mean surface velocity field measured by large-scale particle image velocimetry and velocity profiles. The model was also validated against metrics derived from the aerial drone video taken on July 9^{th}, 2020, specifically the location and spatial scales of the primary streamwise orientated vortices and the frequencies and lateral scales of the large-scale episodic pulses (see Figs. 6 and 7 of Duguay et al. (2022)). These validations establish confidence in the model's ability to provide insights on coherent flow structure formation and interactions.

3 Results

3.1 Instantaneous flow field

The left-hand panels of Fig. 3 show plan views of the typical instantaneous flow structure of the mixing interface for each case. The 3D contours were generated from isocontours of α defining the interface between the waters of the Coaticook and the Massawippi. The contours are coloured by vertical velocity (w) to indicate the sense of streamwise rotation of the structures. Contours of $\alpha > 0.9$ retain flow predominantly from the Coaticook and $\alpha < 0.1$ retain flow predominantly from the Massawippi. A distinct line on the surface is visible in each case (3). This line is the *partition line* and its real-world analogue is also clearly visible in aerial drone imagery of the confluence (see Fig. 5 of Duguay et al. (2022)).

In the $\overleftarrow{\Delta\rho}$ simulations (Fig. 3a-c), the denser Coaticook slides under the lighter Massawippi to the left of the partition line (i.e. towards the left bank), extending farther into the Massawippi with increasing magnitude of $\Delta\rho$. The same is true, yet in the opposite lateral direction in the $\overrightarrow{\Delta\rho}$ simulations (Fig. 3d-f). The $\Delta\rho_{0.0}$ case often develops large anticlockwise coherent SOVs on the Coaticook side of the partition line (Fig. 3d). However, when a $\Delta\rho$ is considered, either this anticlockwise secondary flow is reinforced (i.e. a dense Massawippi sliding underneath a light Coaticook, $\overrightarrow{\Delta\rho}$, Fig. 3e-f) or is inverted, causing clockwise secondary motion to form on the Massawippi side of the partition line (i.e. dense Coaticook sliding under a light Massawippi, $\overleftarrow{\Delta\rho}$, Fig. 3a-c). In the left-hand panels, the α contours of the $\overleftarrow{\Delta\rho}$ simulations 'close over' producing coherent, near circular density SOVs similar to those observed in the aerial video of Duguay et al. (2022). However,

in the $\overrightarrow{\Delta\rho}$ cases, the α contours do not close over, instead they develop numerous upwelling red coloured 'cusps' adjacent to deep blue coloured cavities. These cusps indicate interfacial instabilities spread along the interface of the dense Massawippi and light Coaticook.

Animations of α (see Video 2 and Video 3) show the secondary flow of the $\overleftarrow{\Delta\rho}_{0.5}$ case is often contained within well-defined circular SOVs, whereas in the $\overrightarrow{\Delta\rho}_{0.5}$ case, the mixing interface is characterised by less spatiotemporally coherent, more chaotic secondary flow structures. The coherence of the SOVs in the $\overleftarrow{\Delta\rho}_{0.5}$ case is explained by the lighter Massawippi *slowly* moving overtop the dense front of the Coaticook. In contrast, the fast flow of the Coaticook in the $\overrightarrow{\Delta\rho}_{0.5}$ case rapidly moves overtop the dense Massawippi, shearing the mixing interface in the process (best observed in Video 3). This shearing produces numerous 'cusped' interfacial instabilities. This difference in the secondary flow field is caused only by the change in direction of $\Delta\rho$, which shows the inertia of the tributary opposing the dense front dictates whether the secondary flow field will be characterised by large elliptical/circular density SOVs or more erratic interfacial instabilities mingled with the occasional density SOV.

3.2 Space-time matrices

The coherence of secondary flow structure and the growth of these structures is apparent in the space-time matrices of Fig. 4. These matrices were constructed from digital renders of the confluence's mixing interface using the same method described in Section 4.1 and 4.2 of Duguay et al. (2022) and they provide a 'temporal' view of coherent flow structures passing through a cross section of the mixing interface ($x = 4$ m). The dynamics of episodic pulses in the mixing interface vary with the magnitude and direction of $\Delta\rho$. The partition lines (sharp gradient delineating the solid grey free surface from the subsurface billows) visible in the space-time matrices of Fig. 4 convey this variability. The maximum lateral displacements of the partition line increase in frequency in the $\overleftarrow{\Delta\rho}$ simulations with increasing magnitude of $\Delta\rho$. Also, it becomes increasingly difficult to discern large amplitude episodic pulses in the space-time matrices for magnitudes of $\overleftarrow{\Delta\rho}$ greater than 0.5 kg/m^3 such as those visible in $\Delta\rho_{0.0}$ and $\overleftarrow{\Delta\rho}_{0.5}$ (and drone video of Duguay et al. (2022)). For example, the partition line takes on a more serrated character in the $\overrightarrow{\Delta\rho}_{0.5}$ case compared to the $\overleftarrow{\Delta\rho}_{0.5}$ case, noted by the smaller amplitudes and more frequent lateral displacements of the partition line. The $\overrightarrow{\Delta\rho}$ simulations also lack the pronounced episodic pulses observed in the $\Delta\rho_{0.0}$ and $\overleftarrow{\Delta\rho}_{0.5}$ cases. Finally, the splaying behaviour of the primary SOV as it interacts with the free

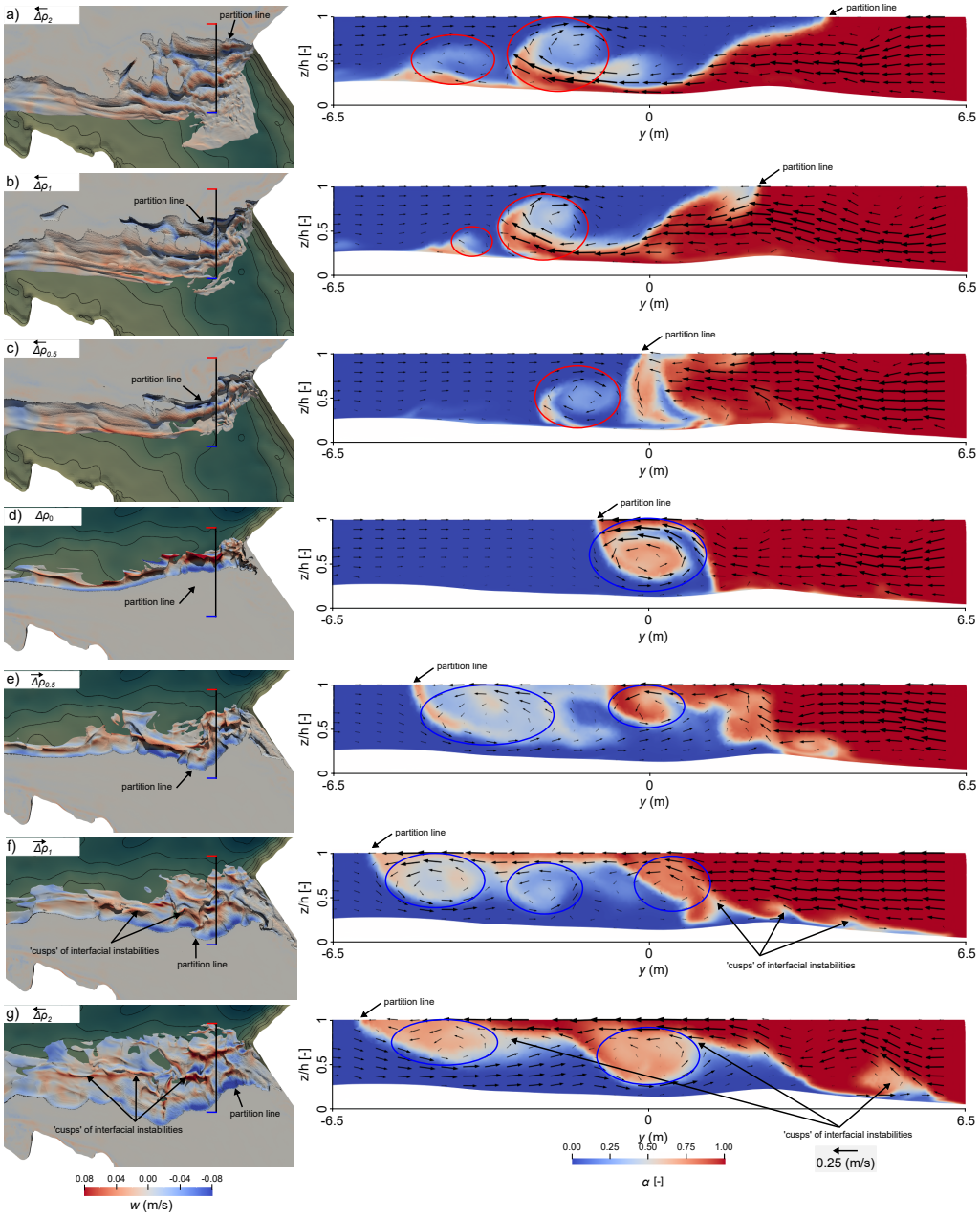

Figure 3. Left-hand panels depicting typical instantaneous flow structure revealed by isocontours of α coloured by vertical velocity (w). Right-hand panels present cross-sections at $x = 4$ m (identified as black lines in the left-hand panels) of characteristic instantaneous α fields with secondary velocity vectors. Red and blue colouring of α in the right-hand panels indicate flow from the Coaticook and Massawippi respectively. a-g) Typical instantaneous results for the $\overleftarrow{\Delta\rho}_{2.0}$, $\overleftarrow{\Delta\rho}_{1.0}$, $\overleftarrow{\Delta\rho}_{0.5}$, $\Delta\rho_{0.0}$, $\overrightarrow{\Delta\rho}_{0.5}$, $\overrightarrow{\Delta\rho}_1$ and $\overrightarrow{\Delta\rho}_{2.0}$ cases respectively. Red ellipses indicate clockwise rotating secondary flow structure whereas blue ellipses indicate anticlockwise secondary flow patterns.

surface is apparent in case $\overleftarrow{\Delta\rho}_{0.5}$ and to a greater degree in cases $\overleftarrow{\Delta\rho}_{1.0}$ and $\overleftarrow{\Delta\rho}_{2.0}$ (Fig. 4). No such splaying behaviour is observed on the Coaticook side in the $\overrightarrow{\Delta\rho}$ cases indicating that upwelling billows of dense Massawippi do not reach the free surface as they do in the $\overleftarrow{\Delta\rho}$ cases.

3.3 Mean flow field

Cross-sections of the mean flow field show how $\Delta\rho$ affects the mixing interface's structure (Fig. 5a). The tilt of the mixing interface increases with the magnitude of $\Delta\rho$, regardless of its direction (Fig. 5a). However, in the $\Delta\rho_{0.0}$ case, the mixing interface also tilts slightly towards the left bank (Massawippi side). Because $\Delta\rho$ is absent in this case, this tilt is attributed to the greater near-surface lateral velocities of the Coaticook deflecting the slower flow of the Massawippi to the left (see Fig. 5c). In the $\overleftarrow{\Delta\rho}$ cases, vectors projected from the mean 3D flow field onto the slices show clockwise secondary flow motions (red ellipses) in Fig. 5a. In contrast, anticlockwise motions (blue ellipses) develop in the $\overrightarrow{\Delta\rho}$ cases. In all cases, independent of the direction of $\Delta\rho$, the secondary motions appear approximately at the same lateral position as the SOVs in the aerial drone video of Duguay et al. (2022) (see underlay of Fig. 4a). The widths of the SOVs in the $\overleftarrow{\Delta\rho}$ cases increase with the magnitude of $\Delta\rho$ and a smaller secondary SOVs appears adjacent to the primary SOV in the $\overleftarrow{\Delta\rho}_{0.5}$ simulation. Similar, though wider, secondary SOVs also appear adjacent to the primary SOVs in the $\overleftarrow{\Delta\rho}_{1.0}$ and $\overleftarrow{\Delta\rho}_{2.0}$ simulations. Whereas the mean secondary motions in the $\overleftarrow{\Delta\rho}$ cases are mostly attributed to spatiotemporally coherent density SOVs, the mean motions in the $\overrightarrow{\Delta\rho}$ cases are mostly attributed to interfacial instabilities. This difference is best conveyed in Video 2. Finally, coherent SOVs are absent in the mean flow field of the $\Delta\rho_{0.0}$ case (Fig. 5a), despite such motions being observed in the instantaneous flow field of Fig. 3d. Their absence is attributed to the temporal averaging of the lateral movements of the episodic pulses.

Distributions of $\overline{u}$ (overbar indicates time averaged) are similar across the cases (Fig. 5b). However, in Fig. 5b the $\Delta\rho_{0.0}$ case has the lowest $\overline{u}$. Also, $\overline{u}$ increases on the Massawippi side with increasing magnitude of $\Delta\rho$, irrespective of its direction. These increases are caused by greater mixing of the Coaticook's streamwise momentum along the increasingly tilted mixing interface as $\Delta\rho$ strengthens. A region of high $\overline{u}$ on the Coaticook side migrates progressively from near the bed in $\overleftarrow{\Delta\rho}_2$ to near the surface in $\overrightarrow{\Delta\rho}_2$. The fast dense downwelling flow of the Coaticook in the $\overleftarrow{\Delta\rho}_2$ case causes this high $\overline{u}$ near the bed, whereas the

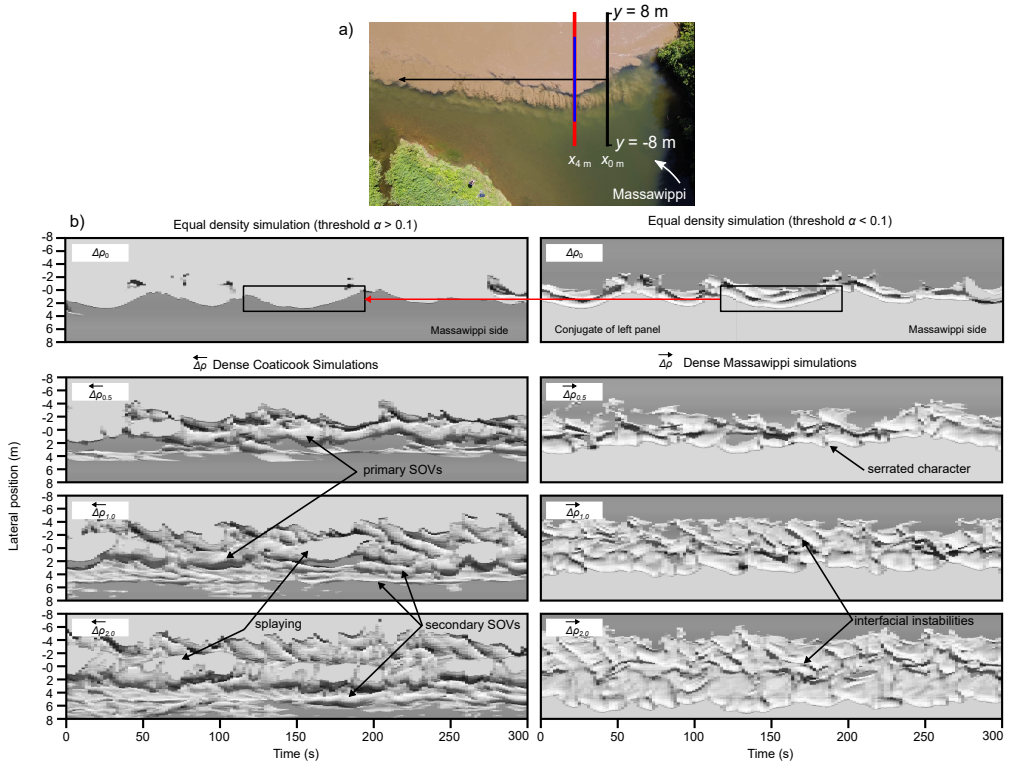

Figure 4. Space-time matrices derived from numerical planview renders of α contours (e.g. similar to those on the left-hand side of Fig. 3). a) Red line indicates the streamwise position and lateral extents of the sampling rectangle used to extract image data. Photo presents an aerial view of the mixing interface on July 9^{th}, 2020 showing the location of the mixing interface and density SOV. b) Numerical space-time matrices for the equal density ($\Delta\rho_{0.0}$) simulation (top-row, right panel is the conjugate of the left panel for the same conditions). Lower rows show the effect of increased $\Delta\rho$ on vertical stratification of the mixing interface, the size of the primary SOVs, higher-order SOVs, interfacial instabilities and episodic pulses. Splaying behaviour of the primary SOVs visible as flat spots at the free surface. Black rectangles show the passage of a coherent anticlockwise rotating SOV in each α threshold of the $\Delta\rho_{0.0}$ case. Digital renders used to produce the matrices were sampled from results at a frequency of 0.5 Hz. Shadow casting in post-processing provides a realistic perspective of depth.

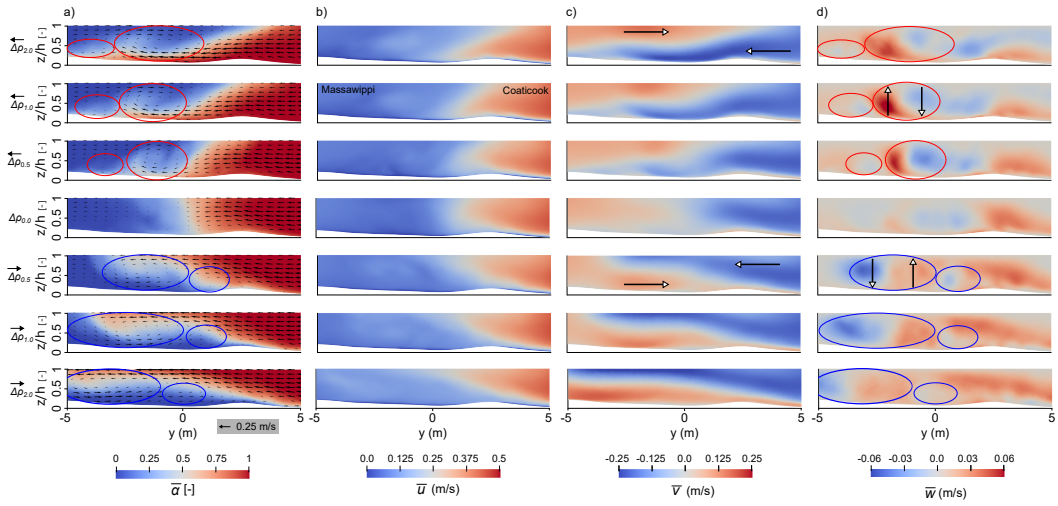

Figure 5. Cross-sections of mean flow field characteristics taken at $x = 4$ m (streamwise position and lateral extents indicated by the blue line in Fig. 4a). a) Mean α ($\overline{\alpha}$) for each $\Delta\rho$ case with secondary flow vectors. Red and blue ellipses respectively indicate clockwise and anticlockwise secondary flow motions. b) Mean streamwise velocity component ($\overline{u}$, flow into page), c) mean lateral component ($\overline{v}$) and, d) mean vertical component ($\overline{w}$).

slow dense downwelling Massawippi in the $\overrightarrow{\Delta\rho}_2$ case causes the fast light Coaticook to move towards the surface. The faster streamwise velocities of the Coaticook (Fig. 5b) shear the dense front of the Massawippi causing the interfacial instabilities in the $\overrightarrow{\Delta\rho}$ cases. The fast overtopping Coaticook also prevents the upwelling billows of dense Massawippi from attaining the free surface, explaining the absence of splaying behaviour in the space-time matrices of the $\overrightarrow{\Delta\rho}$ cases (Fig. 4). Finally, vertical velocities reveal upwelling regions adjacent to downwelling regions in the $\overleftarrow{\Delta\rho}$ and $\overrightarrow{\Delta\rho}$ cases between $\approx$ -5 $< y <$ 0 in Fig. 5d.

3.4 Mixing

Mixing can be assessed by examining distributions of the standard deviation of α (σ_α) and their products with the standard deviations of each of the three velocity components (Figure 6). In Fig. 6a, regions of high σ_α signify regions of intense mixing which stretch laterally with increasing $\Delta\rho$ owing to greater flow stratification. In all cases, the variability of the lateral velocity component (v) seems to predominantly drive mixing, with $\sigma_\alpha\sigma_v$ greater than both $\sigma_\alpha\sigma_u$ and $\sigma_\alpha\sigma_w$ (Fig. 6c). Curiously, the greatest values of $\sigma_\alpha\sigma_v$ occur in the $\overleftarrow{\Delta\rho}_{0.5}$ and $\overleftarrow{\Delta\rho}_1$ cases and the widest swath of high $\sigma_\alpha\sigma_v$ appears in the $\Delta\rho_{0.0}$ case. These

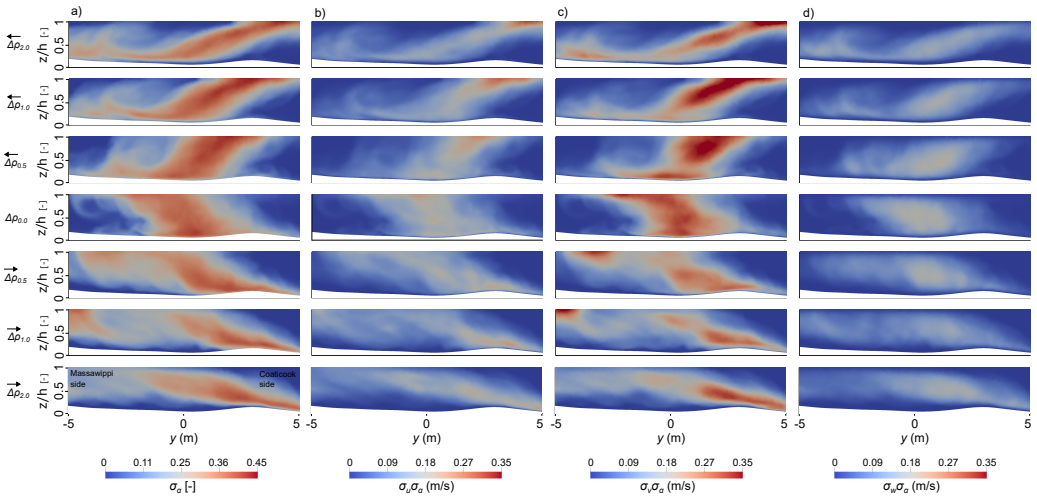

Figure 6. a) Distributions of the standard deviation of α (σ_α) over a cross-section at $x = 4$ m (streamwise position and lateral extents indicated by the blue line in Fig. 4a). b) Product of σ_α with the standard deviation of the streamwise component u ($\sigma_\alpha\sigma_u$). c) Product of σ_α with the standard deviation of the lateral component ($\sigma_\alpha\sigma_v$). d) Product of σ_α with σ_w ($\sigma_\alpha\sigma_w$).

high values are attributed to the strong lateral movements of the pronounced episodic pulses present in these cases (Fig. 4). For the $\overrightarrow{\Delta\rho}_{0.5}$ case, $\sigma_\alpha\sigma_v$ values are smaller, attributable to interfacial instabilities along the mixing interface rather than the lateral movements of episodic pulses (see Fig. 3e-g and Video 3). The product $\sigma_\alpha\sigma_w$ develops a characteristic curl where the coherent density SOVs occur in the $\overleftarrow{\Delta\rho}$ cases (also apparent in the $\sigma_\alpha\sigma_v$ panels). In the $\overrightarrow{\Delta\rho}$ cases, regions of high $\sigma_\alpha\sigma_w$ appear where the anticlockwise secondary flow structures develop.

The increase of mixed α flux (Q_{mixed}) downstream of the apex (Fig. 7) is also a useful metric to examine mixing rates. Flux is considered mixed when $\overline{\alpha}$ is between 0.05 and 0.95 (i.e. containing at least 5% and a maximum of 95% of Coaticook by volume). To calculate Q_{mixed}, cross-sections separated longitudinally by 1 m along the streamwise direction beginning at the confluence's apex are trimmed (*thresholded*) to remove cross-sectional area outside of the $\overline{\alpha}$ bounds. The flux of the mixed fluid through the retained surface is then calculated with Eq. 6, where dS is the retained surface, $\overline{\mathbf{u}}$ is the mean 3D velocity vector and $\mathbf{n}$ is the normal vector on dS. Q_{mixed} is normalised by the confluence's total discharge to obtain the fraction of mixed discharge (Q^*, Eq. 7, where $Q^* = 1$ would indicate complete mixing). Q^* increases with the magnitude of $\Delta\rho$ (Fig. 7) independent

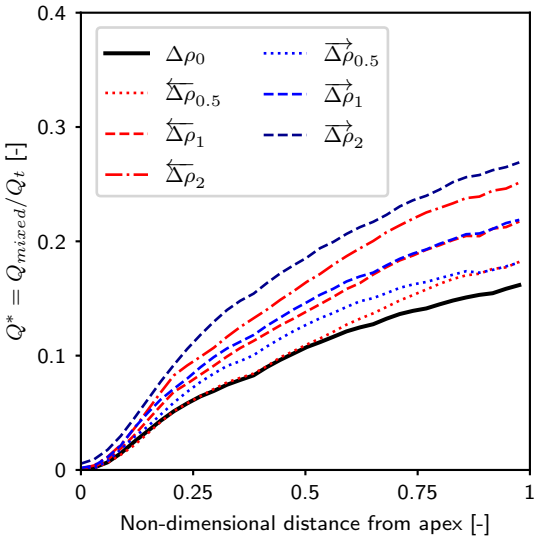

Figure 7. Variation in the flux of mixed fluid (Q^*) with non-dimensional distance from the confluence apex (non-dimensionalized by downstream width, $B = 33.8$ m) for the 7 studied configurations of $\Delta\rho$.

of the direction of the density gradient. For the two smaller magnitudes of $\Delta\rho$, the profiles of Q^* are similar for both directions of $\Delta\rho$. The sharp increase in Q^* between the $\Delta\rho_{0.0}$ case and the $\Delta\rho = 2$ kg/m^3 cases (both directions) is attributed to the additional interfacial mixing area caused by greater flow stratification. Some of the greater mixing observed in the $\overrightarrow{\Delta\rho}$ compared to their $\overleftarrow{\Delta\rho}$ counterparts is likely due to the shearing effect of the fast Coaticook overtop the dense front of the Massawippi causing the interfacial instabilities dominant in the $\overrightarrow{\Delta\rho}$ cases.

$$Q_{mixed} = \int_S \overline{\mathbf{u}} \cdot \mathbf{n} dS \tag{6}$$

$$Q^* = \frac{Q_{mixed}}{Q_t} \tag{7}$$

4 Discussion

Our results show that small magnitudes of $\Delta\rho$ strongly modify secondary flow structure in the mixing interface of the Coaticook-Massawippi confluence. A $\Delta\rho$ of only 0.5 kg/m^3, or

≈ 0.05 % the density of water at 24.5°C, was sufficient to invert the sense of rotation of the secondary flow structure (anticlockwise to clockwise) and the tilt of the mixing interface. Inertial effects were also very important. For the same magnitude of $\Delta\rho$ the mixing interface can either produce coherent density SOVs or interfacial instabilities depending on whether the dense front collides with the *slow* Massawippi or the *fast* Coaticook tributary. Because all variables in the simulated cases were constant, except the magnitude and direction of $\Delta\rho$, the sensitivity of the mixing interface to these commonly occurring magnitudes of $\Delta\rho$ (<2 kg/m^3) suggests that $\Delta\rho$ and its direction are the dominant parameters driving secondary flow structure within the mixing interface. Following a discussion on direction effects on secondary flow structure, we elaborate on this last statement with the following three points.

First, we provide an explanation for how weak values of $\Delta\rho$ fundamentally alter the flow field to physically prevent dual back-to-back SOVs from forming. Second, a temperature analysis of the Coaticook and Massawippi rivers shows how the direction of $\Delta\rho$ can switch on a diurnal basis, highlighting the importance of thermal gradients on secondary flow structure. Third, aerial observations of anticlockwise rotating SOVs at the Coaticook-Massawippi are presented and discussed to support the numerical predictions of similar anticlockwise SOVs in the $\Delta\rho_{0.0}$ case (Fig. 3d-g). Taken together with our results, these points convey that $\Delta\rho$ and its direction are *key*, rather than incidental parameters in shaping secondary flow structure in the mixing interface at the Coaticook-Massawippi confluence, and in all likelihood, at many other river confluences as well. Finally, a convention for calculating $\mathbf{F}_D$ is proposed to account for the direction of $\Delta\rho$ to capture the effects of the light tributary's inertia on the dense tributary's protruding dense front.

4.1 Impact of the direction of $\Delta\rho$ on secondary flow structure

As shown in Fig. 8b, even the $\approx$ 2x to 3x greater velocities on the Coaticook side were unable to impede the lateral extension of the dense front of the Massawippi in the $\overrightarrow{\Delta\rho}_{0.5}$ case (see also Figs. 3e-g). This indicates the $\Delta\rho$ pressure gradient developed by the denser Massawippi was sufficient to overcome the opposing inertial forces of the Coaticook. Similar behaviour is likely to occur for other common momentum ratios at the confluence (and at other sites). The direction of $\Delta\rho$ therefore determines the dominant sense of rotation of secondary flow in the mixing interface. Moreover, as can also be observed in Fig. 8, the character of the instantaneous secondary flow motion is strongly affected by the inertia of the tributary opposing the dense front. In the case of $\overleftarrow{\Delta\rho}_{0.5}$, near circular density SOVs

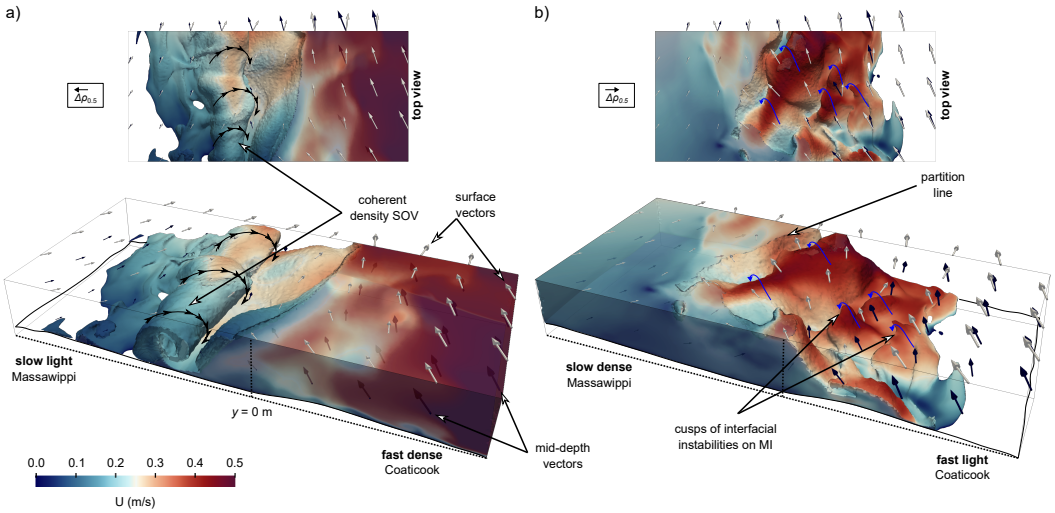

Figure 8. Conceptual effects of the direction of $\Delta\rho_{0.5}$ on the mixing interface's flow structure. a) A top and oblique view of a typical instantaneous $\alpha > 0.9$ field (i.e. mostly unmixed Coaticook) from the $\overleftarrow{\Delta\rho}_{0.5}$ case coloured by velocity magnitude. Coherent density SOVs characterise this case where a fast-dense Coaticook encounters a slow-light Massawippi. Rotation of the density SOV is indicated by black arrows. Opacity permits near-surface (light gray) and mid-depth (dark blue) velocity vectors scaled by velocity magnitude to be viewed. b) Similar to (a) yet of the $\overrightarrow{\Delta\rho}_{0.5}$ case with a $\alpha < 0.1$ (i.e. mostly unmixed Massawippi). Numerous 'cusps' indicate interfacial instabilities (blue arrows) caused by shear between the dense front of the Massawippi and the fast light front of the Coaticook. The high values of U (velocity magnitude) on the α contours on the Coaticook side are indicative of the shearing process responsible for forming the interfacial instabilities. Video 3 presents a side-by-side animation of (a) and (b) to better convey the mixing interface dynamics.

develop when the dense Coaticook collides with the lower velocity Massawippi (animated in Video 3). In contrast, interfacial instabilities and much less spatiotemporally coherent density SOVs form in the $\overrightarrow{\Delta\rho}_{0.5}$ case where the dense front of the Massawippi encounters the fast Coaticook (animated in Video 3). Similar patterns develop with greater magnitudes of $\Delta\rho$ (not shown), with the main differences being increased stratification and wider density SOVs (see space-time matrices of Fig. 4a).

4.2 Causal mechanisms of density SOVs

The formation of SOVs has largely been attributed to the downwelling of superelevated flow mechanism (DSF) (Paola, 1997; Constantinescu et al., 2011, 2012; Constanti-

nescu, 2014; Constantinescu et al., 2016; Cheng & Constantinescu, 2018; Sukhodolov & Sukhodolova, 2019; Horna-Munoz et al., 2020). As the opposing flows collide near the apex, a portion of their kinetic energy converts to potential energy (i.e. superelevated surface), which subsequently converts back to kinetic energy as the superelevated mass is accelerated towards the bed. The DSF mechanism is purported to produce two back-to-back, surface convergent, counter-rotating SOVs, one flanking each side of the mixing interface (Constantinescu et al., 2011; Sukhodolov & Sukhodolova, 2019) and is suggested to be the dominant driver of streamwise vorticity within the mixing interface of river confluences. Based on our work of the Coaticook-Massawippi confluence, we propose that even small values of $\Delta\rho$, by inciting the confined gravity current mechanism described by Duguay et al. (2022), likely overrides the DSF mechanism, resulting in a predominantly buoyancy driven secondary flow field in the mixing interface.

The secondary flow structures of the $\overrightarrow{\Delta\rho}$ and $\overleftarrow{\Delta\rho}$ cases in Fig. 3, despite often sharing similar lateral locations, appear on opposite sides of the partition line, at opposite positions above the bed and rotate in opposite senses. These opposites occur because the SOVs form from fundamentally different hydrodynamic processes - near-bed downwelling of the Massawippi in $\overrightarrow{\Delta\rho}_{0.5}$ versus near-bed downwelling of the Coaticook in $\overleftarrow{\Delta\rho}_{0.5}$ (Fig. 8 and Videos 2 and 3). Because the unbalanced density driven hydrostatic pressure distribution across the partition line perpetually pushes fluid from one side of the mixing interface to the other, the formation of dual, back-to-back, counterrotating SOVs is prevented. Stated otherwise, the hypothetically *paired* SOV on the dense side of the partition line - expected if the DSF mechanism was dominant - physically cannot form because of the continuous lateral flow under the partition line. Evidence of this perpetual lateral flow and absence of paired SOV is presented in Figs. 3 and 5.

The remarkable differences due to the $\Delta\rho$ direction depicted in Fig. 8 combined with the fact that similarly small magnitudes of $\Delta\rho$ are often, if not always, present at the Coaticook-Massawippi confluence, suggests that $\Delta\rho$ and its direction are the controlling mechanism of secondary flow patterns in its mixing interface. However, this does not mean that the DSF mechanism doesn't influence the process, rather it is unclear to what extent it may enhance or detract from the confined gravity current mechanism. One possibility is that the energy that would normally be transferred into the paired SOV is instead advected into the density SOV to accentuate its circulation. Additional research on this topic is required

and eddy resolved numerical modelling accounting for free surface deformations could prove promising in this regard.

4.3 Relevance of small temperature differences on $\Delta\rho$

Fluctuations in the temperatures (T) of the Coaticook and Massawippi can result in values of ΔT sufficient to cause important $\Delta\rho$ effects over surprisingly short time-scales. During the summer of 2021, water temperatures were measured at 15 minute intervals in the Coaticook and Massawippi with Solinst Leveloggers (Figure 9). Diurnal temperature fluctuations are discernible between the two rivers over this period. The corresponding values of ΔT and $\Delta\rho$ (calculated with Eq. 9 presented in Duguay et al. (2022)) appear in Fig. 9b,c respectively. Figure 9c suggests fluctuations in $\Delta\rho$ could cause the mixing interface to switch from a $\overleftarrow{\Delta\rho}$ mode in the morning (colder denser Coaticook) to a $\overrightarrow{\Delta\rho}$ (warmer lighter Coaticook) in the late afternoon and evening. The temperature fluctuations are attributed to differences in watershed characteristics affecting their thermal heat budgets (e.g., foliage, incident angle of solar radiation, average width and depth, substrate colour). These diurnal temperature fluctuations suggest that caution should be taken when planning experimental campaigns as velocity measurements taken in the morning would be incompatible with measurements taken in the afternoon as the flow structures could change dramatically (i.e., Fig. 8a in the morning and Fig. 8b in the afternoon). Ignoring these changes would lead to incorrect interpretation of the confluence's secondary flow structure. Similar variations in temperature (and subsequently density) could commonly occur at other confluences. Therefore we suggest temperature measurements be performed at least hourly throughout the experimental campaign and protocols adjusted accordingly if substantial temperature reversals are detected.

4.4 Aerial observations of anticlockwise rotating SOVs

Our numerical modelling predicted anticlockwise rotating SOVs in the $\Delta\rho_{0.0}$ case (Figs. 3d). However until now, only aerial observations of clockwise rotating SOVs have been presented at the Coaticook-Massawippi confluence for $\overleftarrow{\Delta\rho}_{0.5}$ (Duguay et al., 2022). An aerial video filmed on March 18^{th}, 2022 (Video 4) reveals the presence of anticlockwise SOVs. A still image extracted from Video 4 is presented in Fig. 10 with arrows indicating the sense of rotation visible in the movements of the turbidity gradients. The temperatures of the Coaticook and Massawippi at the time of filming were 0.3 °C and 2 °C respectively.

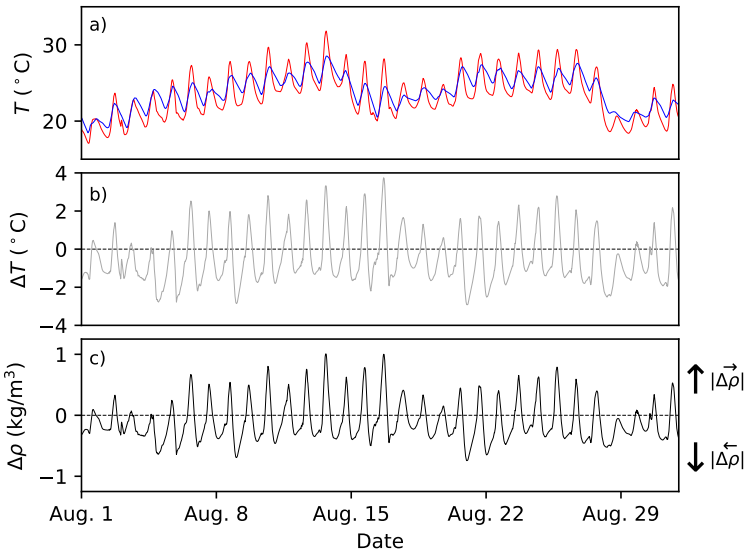

Figure 9. Temporal analysis of $\Delta\rho$ due to diurnal variations in the thermal gradient of the Coaticook-Massawippi confluence. a) Time series showing diurnal fluctuations of T in the Coaticook (red) and Massawippi (blue) rivers for the period between August 1^{st} and September 1^{st} 2021 measured $\approx$ 50 m upstream of the apex in each channel. b) ΔT between the two rivers. Negative values indicate the Coaticook is cooler than the Massawippi. c) Calculated $\Delta\rho$ resulting from ΔT showing $\Delta\rho$ can switch from a $\overleftarrow{\Delta\rho}$ scenario to a $\overrightarrow{\Delta\rho}$ scenario over the course of a typical day due to temperature variations in the tributaries.

The suspended sediment concentration (SSC) and water hardness (dissolved $CaCO_3$) for the Coaticook and Massawippi were respectively 212 mg/l, 7.6 mg/l (SSC) and 101 mg/l, 64 mg/l ($CaCO_3$). Combined these water quality parameters result in an $\Delta\rho$ of 0.03 kg/m^3 - thus very nearly a $\Delta\rho_{0.0}$ scenario. The discharge of the Coaticook was 48.9 m^3/s whereas that of the Massawippi was 25.5 m^3/s, for a discharge ratio (Q_r) of 0.52. Whilst this Q_r is less than that modelled herein ($Q_r = 4.65$) the resemblance of the filmed flow structures to those in the $\Delta\rho_{0.0}$ case are striking. It is hypothesized that the anticlockwise SOVs occur due to the stronger near-surface momentum of the Coaticook colliding with the weaker near-surface momentum of the Massawippi. As the faster Coaticook collides with the slower Massawippi, its lateral momentum is reflected downwards while it simultaneously pushes the Massawippi laterally towards the left. This causes the mixing interface to tilt while simultaneously contributing to the development of anticlockwise SOVs (see Fig. 5a and c, $\Delta\rho_{0.0}$). Though the exact processes responsible for the formation of the lone anticlockwise SOV are not fully understood, the observations of March 18th, 2022 are nevertheless consistent with our numerical predictions of such SOVs in the $\Delta\rho_{0.0}$ case. This observation combined with the clockwise SOV observation of Duguay et al. (2022) shows that the same confluence can develop SOVs of opposite sense of rotation when exposed to different density gradient conditions.

4.5 Proposed $\mathbf{F}_D$ convention

Based on our observations and numerical results of the Coaticook-Massawippi confluence, we propose to clarify the definition of $\mathbf{F}_D$ with the following convention: that U_0 be taken as the bulk velocity of the light tributary and that D be a representative depth of the collision zone. This convention makes U_0 represent the inertial forces opposing the lateral propagation of the dense front and provides the researcher flexibility to account for changing field conditions (hydrodynamic and densimetric) during the course of a season long field campaign. The location of D is taken because this is where the unmixed $\Delta\rho$ gradient is strongest, and therefore density effects greatest, and the depth there is also the actual length scale over which stratification occurs. The need to account for the direction of $\Delta\rho$ in $\mathbf{F}_D$ is evident by comparing Fig. 8a with Fig. 8b (and Video 3). The strikingly different mixing interface characteristics apparent in this figure (i.e. coherent density SOVs versus interfacial instabilities) are due solely to the direction of $\Delta\rho$ as the hydraulic conditions and the magnitude of $\Delta\rho$ have not changed. Therefore, it is the light river's inertia which is

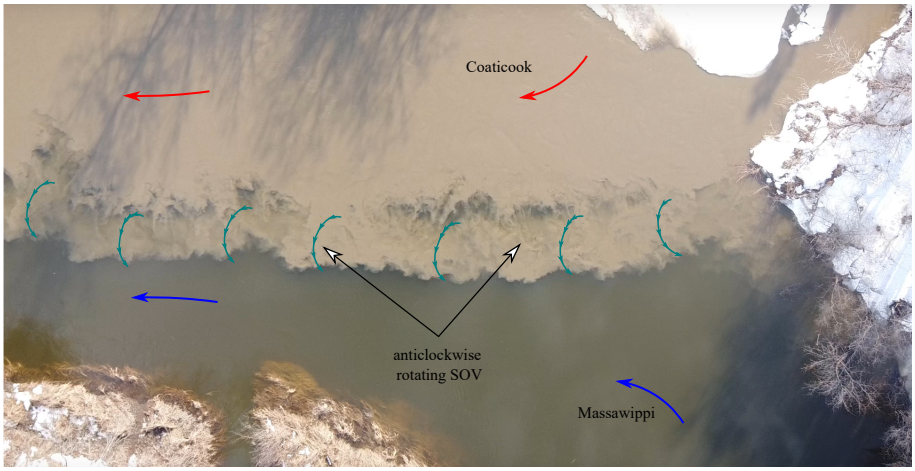

Figure 10. Anticlockwise rotating SOV filmed on March 18^{th}, 2022 at the Coaticook-Massawippi confluence (see Video 4 to observe its motion). The confluence was in a $\Delta\rho_{0.0}$ mode on this date, which was predicted to be conducive of anticlockwise rotating SOVs in our numerical model (see Figs. 3d and 4b top row). Q_C, Q_M and Q_r were respectively 48.9 m^3/s, 25.5 m^3/s and 0.52 on March 18^{th} 2022.

responsible for the differences in secondary flow structure. Importantly, definitions of $\mathbf{F}_D$ based on arbitrarily chosen bulk flow properties such as those presented in Table 1 would result in *a single value* for both the $\overrightarrow{\Delta\rho}_{0.5}$ and $\overleftarrow{\Delta\rho}_{0.5}$ cases in Fig. 8. This single value cannot possibly convey the obvious differences in the secondary flow structure of the two cases, thus illustrating how these definitions lack the necessary subtlety to convey important density gradient direction effects.

The values of $\mathbf{F}_D$ for each of our simulated cases using this convention are presented in Table 4. In the $\overleftarrow{\Delta\rho}$ cases U_0 was taken to be the cross-sectional average velocity of the Massawippi (0.13 m/s) and the cross-sectional average velocity of 0.47 m/s of the Coaticook was used for U_0 in the $\overrightarrow{\Delta\rho}$ cases (both at the apex before the flows enter the confluence). D was taken as 1.6 m. Interpreting our numerical results with the $\mathbf{F}_D$ values of Table 4 suggests that $\mathbf{F}_D$ values between 0.75 and 1.5 are conducive for developing coherent density SOVs (i.e. $\mathbf{F}_D = 0.93$ for $\overleftarrow{\Delta\rho}_{0.5}$) and values larger than 2 and at least up to 5.5 ($\overrightarrow{\Delta\rho}_{2.0}$) can still produce a strong tilt in the mixing interface characterised by interfacial instabilities intermingled with less spatiotemporally coherent SOVs.

Table 4. $\mathbf{F}_D$ values using proposed convention

Case	U_0	D	$\mathbf{F}_D$
$\overleftarrow{\Delta\rho}_{2.0}$	0.13	1.6	0.73
$\overleftarrow{\Delta\rho}_{1.0}$	0.13	1.6	1.04
$\overleftarrow{\Delta\rho}_{0.5}$	0.13	1.6	1.47
$\Delta\rho_{0.0}$	-	-	-
$\overrightarrow{\Delta\rho}_{0.5}$	0.47	1.6	5.30
$\overrightarrow{\Delta\rho}_{1.0}$	0.47	1.6	3.74
$\overrightarrow{\Delta\rho}_{2.0}$	0.47	1.6	2.64

4.5.1 Conceptual description of density and inertial effect interactions

Here we propose a conceptual model, based on numerical modelling and physical reasoning, to describe how density and inertial effects interact to modify secondary flow at river confluences and provide an indication of the potential thresholds of $\mathbf{F}_D$ at which these effects can be expected. This model is based on a symmetric, flat-bed confluence (Fig. 11a) of fixed depth with a denser right channel. The magnitude of $\Delta\rho$ between the two channels is constant, however, the relative velocities of the two tributaries are varied. U_l and U_r are used in the discussion below to indicate the velocities of the left and right channel respectively.

As a first scenario, consider the confluence as a still basin with the waters of both tributaries separated along the mid-axis with no incoming flow. When the fictive barrier separating these waters is removed, the dense right channel will propagate unimpeded along the bed towards the left, and the light channel's waters will move laterally overtop to the right, as expected in a 2D fixed volume lock-exchange (Fig. 11a). This is the case where $\mathbf{F}_D$ tends to 0, either because the opposing tributary has little-to-no momentum or $\Delta\rho$ is very large (or some combination of both).

As a second scenario, consider the left channel to have velocity much less than the right ($U_l << U_r$, Fig. 11b). Now the propagation of the dense front is impeded by the momentum of the left channel by a small degree and the light front is impeded by the momentum of the right channel by a greater degree. A wide ellipsoidal (i.e. depth limited) secondary flow cell forms, composed of at least one but potentially two or more secondary flow cells, as the

light front advances slowly near the surface towards the partition line and the dense front continues to where it is deflected above itself due to the momentum of the left channel (Fig. 11b). Because the fronts are confined by the momentum of their opposing tributaries, this process was described as a 'confined' gravity current by Duguay et al. (2022). The range of $\mathbf{F}_D$ corresponding to the wide ellipsoidal secondary cell scenario is proposed to occur between ≈ 0.2 and 1.

In a third scenario U_l is increased, causing the width of the secondary flow cell to decrease as the dense front encounters greater opposition from the left channel. At a certain value of U_l, the opposing inertia is such that the cell reduces to a near circular density SOV adjacent to the partition line (Fig. 11c), such as that observed by Duguay et al. (2022) and predicted in the $\overleftarrow{\Delta\rho_{0.5}}$ case. These circular density SOVs may be accompanied by smaller higher-order SOVs into the light channel. The range of $\mathbf{F}_D$ corresponding to the circular density SOV scenario is approximately from 0.8 and 1.8.

Values of U_l greater than U_r are considered in the fourth scenario. Now the dense front becomes increasingly sheared and advected downstream (Fig. 8b and Video 3) by the fast overtopping flow of the light channel. Consequently, progressively fewer coherent density SOVs and more interfacial instabilities are expected in the mixing interface for $\mathbf{F}_D$ between ≈ 2 and 6. Periods of intermittent coherent density SOVs followed by interfacial instabilities are expected at the lower end of this range (e.g. $1.8 < \mathbf{F}_D < 4.0$) and as inertial effects begin to dominant at the higher end (e.g. $4.0 < \mathbf{F}_D < 6.0$), progressively less coherent density SOVs are expected as the sheared induced interfacial instabilities begin to dominate.

Finally, as U_l becomes much larger than U_r (e.g. $\mathbf{F}_D > 6$), the propagation of the dense front under the partition line is thwarted as it is near instantly sheared and advected downstream by the fast light flow. A vertical, or near vertical mixing interface, though not modelled herein, likely occurs for values of $\mathbf{F}_D > 7$. When density effects are negligible, coherent SOVs can nevertheless still form as is apparent in Fig. 3d, Fig. 10 and Video 4 due to inertial effects alone. Also, the mixing interface may incline as the fast channel pushes into the slow opposing channel in the collision zone (red ellipse and dotted line in Fig. 11f).

This conceptual understanding of density and inertial effects on the mixing interface using the proposed definition of $\mathbf{F}_D$ is rudimentary in many respects. For instance, it does not account for the influence of other coherent flow structures in the mixing interface nor does it account for the potential effects of superelevated flow (due either to collision or

568 planform curvature). Also, by considering a flat-bed geometry, it does not account for the
569 contribution of scour hole flow separation on the secondary flow field. These two factors
570 likely dominant coherent secondary flow structure as $\mathbf{F}_D$ tends to infinity and but also are
571 expected to alter secondary flow structure in the mixing interface for lower values of $\mathbf{F}_D$ to
572 extents currently unknown.

573 Finally, the need to account for zones of low velocity in the definition of $\mathbf{F}_D$ to capture
574 their potential influence on density SOVs should be assessed in the future. These zones
575 often occur at confluences with high momentum ratios, and their lower velocity potentially
576 favours the production of circular density SOVs. If so, this could mean the bulk cross-
577 sectional average velocity of the light channel may not be the most appropriate value of
578 U_0, and would instead need to be multiplied by a factor to account for the low velocity
579 zone. Irrespective of the current conceptual model's limitations, what is certain from our
580 results is that a $\mathbf{F}_D$ which better incorporates the inertia opposing the propagation of the
581 dense front is necessary to make it a useful metric for assessing the balance between inertial
582 and buoyant effects (as is evident from Fig. 8). Much field, numerical and laboratory
583 work is required to validate the proposed $\mathbf{F}_D$ spectrum, but also to increase its resolution
584 to obtain more certainty of the values of $\mathbf{F}_D$ at which the transitions occur between the
585 various density-driven flow scenarios discussed.

586 5 Conclusions

587 This study used eddy-resolved numerical modelling to show how small density gradients
588 and their direction affect secondary flow structure at the Coaticook-Massawippi confluence
589 where coherent density SOVs were previously observed by Duguay et al. (2022). Reversing
590 the direction of a $\Delta\rho$ of only 0.5 kg/m^3 was sufficient to invert the near-bed lateral flow
591 direction and the sense of rotation of the resulting secondary flow. The development of
592 coherent density SOVs was favoured in cases where a dense-fast Coaticook encountered a
593 slow-light Massawippi. However, when the slow Massawippi was denser, the higher velocities
594 in the light Coaticook sheared the mixing interface, producing interfacial instabilities and
595 less spatiotemporally coherent SOVs. Back-to-back counterrotating SOVs were absent in all
596 cases. Their absence, at least in the $\Delta\rho$ cases, is explained by the perpetual lateral movement
597 of the dense front along the bed physically preventing the paired SOV from forming. It is still
598 unclear how density-induced secondary flow interacts with the downwelling of superelevated
599 flow mechanism and scour hole flow separation to generate the resultant secondary flow

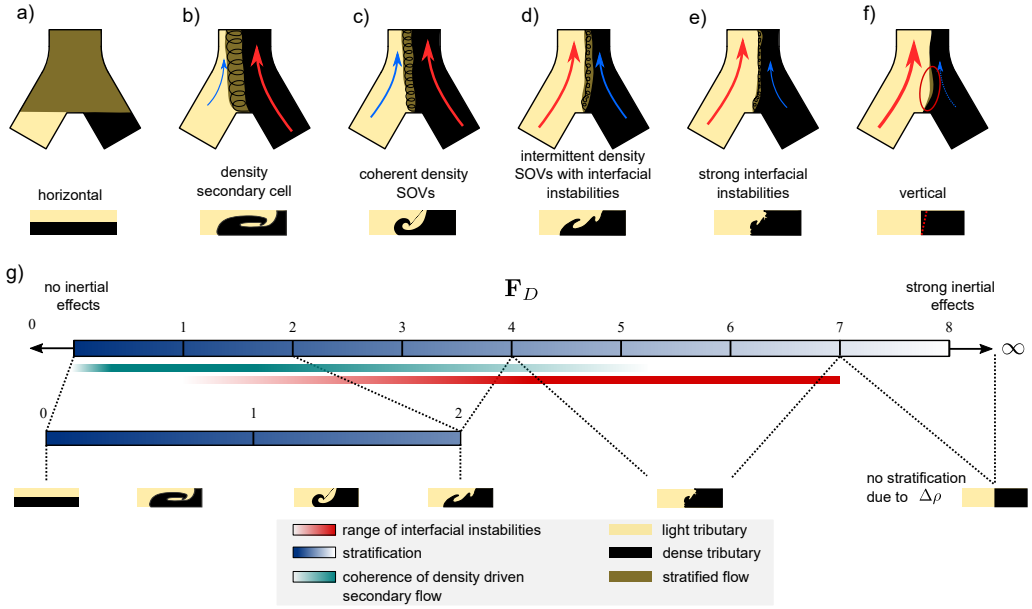

Figure 11. Conceptual model of density and inertial effect interactions. a) Still light (beige) and dense (black) tributaries fully stratify without discharge in both channels. b) Wide density secondary cell forms as the dense front encounters slight opposition from the slow light tributary. c) Near circular coherent density SOVs form with increased opposition from the momentum of the faster light channel. d) Coherence of density SOVs degrades as light channel momentum increases more and begins to shear the stratified mixing interface. e) Strong interfacial instabilities develop as light channel momentum increases further, shearing and advecting the dense front rapidly downstream. f) Mixing interface becomes vertical as dense front cannot overcome the momentum of the light channel. Red ellipse indicates momentum induced tilting. g) Spectrum of conceptual $\mathbf{F}_D$ effects on mixing interface characteristics based on proposed $\mathbf{F}_D$ convention.

field. Additional work is necessary to reconcile these mechanisms with the confined gravity current mechanism in the production of secondary flow.

Time series analysis of water temperatures taken at the Coaticook-Massawippi confluence suggests that its mixing interface can switch from a $\overrightarrow{\Delta\rho}$ mode to a $\overleftarrow{\Delta\rho}$ between the morning and the afternoon. The secondary flow field is largely a function of the magnitude and direction of temperature induced $\Delta\rho$. Diurnal changes imply that velocimetry data sampled in the morning may not be compatible with data sampled in the afternoon which could lead to a misinterpretation of results. It is likely that this process occurs at other mesoscale confluences, and we suggest temperature measurements of the upstream tributaries should be included in all field sampling protocols to assess the consistency of flow conditions.

Given the importance of the direction of $\Delta\rho$ on the mixing interface (i.e. whether the dense front enters a *slow* light channel or a *fast* light channel), a densimetric Froude number ($\mathbf{F}_D$) convention is proposed which explicitly accounts for the inertia of the opposing light channel. The presented $\mathbf{F}_D$ convention and resulting secondary flow spectrum are proposed to better assess how the inertia of the light tributary opposes the propagation of the dense front. Additional field, numerical and laboratory work is still required to validate and refine the proposed $\mathbf{F}_D$ spectrum. Finally, given that small magnitudes of $\Delta\rho$ are commonplace at many natural confluences, it is likely that secondary flow patterns of other mesoscale confluences are also largely dictated by the magnitude and direction of $\Delta\rho$, which would be worth investigating further using this revised $\mathbf{F}_D$ convention.

6 Video captions

6.1 Video 1

A minute of the Coaticook-Massawippi's mixing interface filmed on July 9^{th} 2020 playing at 1x on the left and at 8x on the right (which then repeats 8 times). The rotation of the primary streamwise vortex, made visible by the contrast in turbidity between the two channels, rotates clockwise around a streamwise axis pointing downstream on the clear Massawippi side of the partition line. The coherence of the vortex increases as the episodic pulse from the Coaticook sweeps the SOV towards the left bank of the confluence. A smaller diameter secondary SOV is also observed to form, also with a clockwise sense of rotation to the left of the primary SOV. Near the apex, the dense turbid billows of the Coaticook move laterally left within the lower portion of the water column. This video is also presented and discussed in Duguay et al. (2022).

6.2 Video 2

Cross-sections of α taken at $x = 0$ m (see Fig. 4a) showing the subsurface turbulent flow structure for the (a) $\overleftarrow{\Delta\rho_{0.5}}$ case and the (b) $\overrightarrow{\Delta\rho_{0.5}}$ case. Vectors indicate secondary flow directions resulting from projecting the three-component velocity field onto the cross-section. Red indicates water from the Coaticook, while blue indicates water from the Massawippi. Cross-section is looking downstream. Playback speed of video is 8x. Streamwise vorticity in the $\overleftarrow{\Delta\rho_{0.5}}$ generally occurs clockwise around the streamwise axis facing downstream. In contrast, evidence of anticlockwise streamwise vorticity dominates in the $\overrightarrow{\Delta\rho_{0.5}}$ results.

6.3 Video 3

Animations of contours of α coloured by velocity magnitude to indicate the sense of rotation of the coherent flow structures. Top: α contours indicate flow predominantly from the Coaticook. The presence of strongly coherent streamwise orientated vortices is apparent on the left-hand side of the partition line. Bottom: α contours indicating flow predominantly from the Massawippi. Though coherent streamwise orientated vortices are visible, the fast overtopping flow of the Coaticook is observed to shear the stratified mixing interface, resulting in numerous interfacial instabilities. Yellow vectors indicate instantaneous near-surface flow direction scaled by velocity magnitude. Dark green vectors indicate mid-depth flow direction also scaled by velocity magnitude.

6.4 Video 4

Aerial video of the Coaticook-Massawippi's mixing interface on March 18^{th}, 2022. The dynamics of anticlockwise rotating coherent streamwise orientated vortices are visible. The confluence was under a $\Delta\rho_{0.0}$ mode during filming, which was found to be conducive of anticlockwise rotating SOVs in the numerical modelling performed in this study.

656 ### 6.5 Numerical modelling details

Table 5. Discretization schemes

Dictionary name	Subdictionary	Entry
ddtSchemes		
	default	backward
gradSchemes		
	default	Gauss linear
divSchemes		
	div(rhophi, U)	Gauss vanLeer
	div(phi, alpha)	Gauss limitedLinear01 1
	div(phi,nuTilda)	Gauss upwind
	div((muEff*dev(T(grad(U)))))	Gauss linear
	div((rho*nuEff)*dev2(T(grad(U)))))	Gauss linear
laplacianSchemes		
	default	Gauss linear corrected
interpolationSchemes		
	default	linear

[t]

Table 6. OpenFOAM boundary conditions

field	inlets	outlet	walls	surface	units
nut	zeroGradient	zeroGradient	nutURoughWallFunction	symmetry	[m^2/s]
prgh	zeroGradient	fixedValue 0	zeroGradient	symmetry	[kgm/s^2]
u	turbulentDFSEMInlet	inletOutlet 0	fixedValue 0	symmetry	[m/s]
alpha	fixedValue (1 Coaticook, 0 Massawippi)	zeroGradient	zeroGradient	symmetry	[-]

References

Aguirre-Pe, J., Olivero, M. L., & Moncada, A. T. (2003). Particle densimetric froude number for estimating sediment transport. *Journal of Hydraulic Engineering*, *129*(6), 428-437.

Best, J. L. (1987). Flow dynamics at river channel confluences: Implications for Sediment Transport and Bed Morphology. In *Recent Developments in Fluvial Sedimentology.* SEPM Society for Sedimentary Geology.

Biron, P., Roy, A. G., & Best, J. L. (1996). Turbulent flow structure at concordant and discordant open-channel confluences. *Experiments in Fluids*, *21*, 437-446.

Biron, P. M., & Lane, S. N. (2008). Modelling hydraulics and sediment transport at river confluence. In *River confluences, tributaries and the fluvial network* (pp. 17–43).

Cantero, M. I., Lee, J. R., Balachandar, S., & Garcia, M. H. (2007). On the front velocity of gravity currents. *Journal of Fluid Mechanics*, *586*, 1–39.

Cheng, Z., & Constantinescu, G. (2018). Stratification effects on flow hydrodynamics and mixing at a confluence with a highly discordant bed and a relatively low velocity ratio. *Water Resources Research*, *54*(7), 4537-4562.

Cheng, Z., & Constantinescu, G. (2019). Stratification effects on hydrodynamics and mixing at a river confluence with discordant bed. *Environmental Fluid Mechanics*, *20*, 843–872.

Cheng, Z., & Constantinescu, G. (2021). Shallow mixing layers between non-parallel streams in a flat-bed wide channel. *Journal of Fluid Mechanics*, *916*, 1–37.

Constantinescu, G. (2014). LE of shallow mixing interfaces: A review. *Environmental Fluid Mechanics*, *14*, 971–996.

Constantinescu, G., Miyawaki, S., Rhoads, B., & Sukhodolov, A. (2012). Numerical analysis of the effect of momentum ratio on the dynamics and sediment-entrainment capacity of coherent flow structures at a stream confluence. *Journal of Geophysical Research: Earth Surface*, *117*, 1–21.

Constantinescu, G., Miyawaki, S., Rhoads, B., & Sukhodolov, A. (2016). Influence of planform geometry and momentum ratio on thermal mixing at a stream confluence with a concordant bed. *Environmental Fluid Mechanics*, *16*, 845–873.

Constantinescu, G., Miyawaki, S., Rhoads, B., Sukhodolov, A., & Kirkil, G. (2011). Structure of turbulent flow at a river confluence with momentum and velocity ratios close to 1: Insight provided by an eddy-resolving numerical simulation. *Water Resources*

Research, *47*, 1–16.

Cook, C. B., & Richmond, M. C. (2004). Monitoring and simulating 3-d density currents at the confluence of the snake and clearwater rivers. In *Critical transitions in water and environmental resources management* (p. 1-9).

Dorrell, R., Peakall, J., Sumner, E., Parsons, D., Darby, S., Wynn, R., ... Tezcan, D. (2016). Flow dynamics and mixing processes in hydraulic jump arrays: Implications for channel-lobe transition zones. *Marine Geology*, *381*, 181-193.

Duguay, J., Biron, P., & Lacey, J. (2022). Direct observations of density-driven streamwise oriented vortices at a river confluence. *In review: Water Resources Research*. doi: doi.org/10.1002/essoar.10508854.1

Grbčič, L., Kranjčević, L., Lučin, I., & Čarija, Z. (2019). Experimental and numerical investigation of mixing phenomena in double-Tee junctions. *Water (Switzerland)*, *11*(6).

Gruber, M. F., Johnson, C. J., Tang, C. Y., Jensen, M. H., Yde, L., & Hélix-Nielsen, C. (2011). Computational fluid dynamics simulations of flow and concentration polarization in forward osmosis membrane systems. *Journal of Membrane Science*, *379*(1-2), 488–495.

Gualtieri, C., Ianniruberto, M., & Filizola, N. (2019). On the mixing of rivers with a difference in density: The case of the Negro/Solimões confluence, Brazil. *Journal of Hydrology*, *578*(August).

Horna-Munoz, D., Constantinescu, G., Rhoads, B., Lewis, Q., & Sukhodolov, A. (2020). Density effects at a concordant bed natural river confluence. *Water Resources Research*, *56*.

Jiang, C., Constantinescu, G., Yuan, S., & Tang, H. (2022). Flow hydrodynamics, density contrast effects and mixing at the confluence between the Yangtze and the Poyang Lake channel. *Environmental Fluid Mechanics*.

Lai, A. C., Zhao, B., Law, A. W. K., & Adams, E. E. (2015). A numerical and analytical study of the effect of aspect ratio on the behavior of a round thermal. *Environmental Fluid Mechanics*, *15*(1), 85–108.

Lane, S. N., Parsons, D. R., Best, J. L., Orfeo, O., Kostaschuk, R. A., & Hardy, R. J. (2008). Causes of rapid mixing at a junction of two large rivers: Río Paraná and Río Paraguay, Argentina. *Journal of Geophysical Research: Earth Surface*, *113*, 1–16.

Lindenschmidt, K. E. (2017). RIVICE-A non-proprietary, open-source, one-dimensional

723 river-ice model. *Water (Switzerland)*, *9*(5).

724 Lyubimova, T., Lepikhin, A., Konovalov, V., Parshakova, Y., & Tiunov, A. (2014). For-
725 mation of the density currents in the zone of confluence of two rivers. *Journal of*
726 *Hydrology*, *508*, 328–342.

727 Moukalled, F., Mangani, L., & Darwish, M. (2016). *The finite volume method in computa-*
728 *tional fluid dynamics* (Vol. 113). Springer International Publishing.

729 Paola, C. (1997). When streams collide. *Nature*, *387*, 232–233.

730 Ramón, C. L., Armengol, J., Dolz, J., Prats, J., & Rueda, F. J. (2014). Mixing dynamics
731 at the confluence of two large rivers undergoing weak density variations. *Journal of*
732 *Geophysical Research: Oceans*, *119*, 2386-2402.

733 Ramón, C. L., Prats, J., & Rueda, F. J. (2016). The influence of flow inertia, buoyancy,
734 wind, and flow unsteadiness on mixing at the asymmetrical confluence of two large
735 rivers. *Journal of Hydrology*, *539*, 11-26.

736 Rhoads, B. L. (2020). The Dynamics of River Confluences. In *River dynamics: geomor-*
737 *phology to support management* (pp. 269–293). Cambridge University Press.

738 Rhoads, B. L., & Sukhodolov, A. N. (2001). Field investigation of three-dimensional flow
739 structure at stream confluences: 1. Thermal mixing and time-averaged velocities. *Wa-*
740 *ter Resources Research*, *37*, 2393–2410.

741 Rottman, J. W., & Simpson, J. E. (1983). Gravity currents produced by instantaneous
742 releases of a heavy fluid in a rectangular channel. *Journal of Fluid Mechanics*, *135*,
743 95–110.

744 Sabrina, S., Lewis, Q., & Rhoads, B. (2021). Large-scale particle image velocimetry reveals
745 pulsing of incoming flow at a stream confluence. *Water Resources Research*, *57*(9),
746 e2021WR029662.

747 Sukhodolov, A. N., & Rhoads, B. L. (2001). Field investigation of three-dimensional flow
748 structure at stream confluences: 2. Turbulence. *Water Resources Research*, *37*, 2411–
749 2424.

750 Sukhodolov, A. N., & Sukhodolova, T. A. (2019). Dynamics of flow at concordant gravel
751 bed river confluences: Effects of junction angle and momentum flux ratio. *Journal of*
752 *Geophysical Research: Earth Surface*, *124*, 588–615.

753 van Rooijen, E., Mosselman, E., Sloff, K., & Uijttewaal, W. (2020). The effect of small
754 density differences at river confluences. *Water (Switzerland)*, *12*, 1–18.

755 Weller, H. G., Tabor, G., Jasak, H., & Fureby, C. (1998). A tensorial approach to computa-

tional continuum mechanics using object-oriented techniques. *Computers in Physics*, *12*, 620-631.

Zhang, S., Jiang, B., Law, A. W. K., & Zhao, B. (2016). Large eddy simulations of 45° inclined dense jets. *Environmental Fluid Mechanics*, *16*(1), 101–121.